crystals

MDPI

Article

Evolution Mechanism of Transient Strain and Residual Stress Distribution in Al 6061 Laser Welding

Youmin Rong [1,2,*], Yu Huang [1,2] and Lu Wang [1,2]

[1] State Key Lab of Digital Manufacturing Equipment and Technology, Huazhong University of Science and Technology, Wuhan 470074, China; yuhuang_hust@hust.edu.cn (Y.H.); m201970520@hust.edu.cn (L.W.)
[2] School of Mechanical Science and Engineering, Huazhong University of Science and Technology, Wuhan 430074, China
* Correspondence: ymrong1987@gmail or rym@hust.edu.cn

Abstract: Considering the harm that residual stress causes to the mechanical properties of a weld joint, the evolution mechanisms of transient strain and residual stress distribution are investigated in laser welding of Al 6061, considering that these originate from non-uniform temperature distribution and are intensified further by the unbalanced procedure of melting and solidification. Thermal-elastic-plastic finite element method is developed and analyzed, while the actual weld profile is novel fitted by a B-spline curve. Transient strain is extracted by strain gauges. Longitudinal strain starts from a fluctuating compressive state and progresses to an ultimate residual tension state at the starting and ending welding positions, respectively. The maximum fitting deviation of the weld profile is 0.13 mm. Experimental and simulation results of residual strain are 842.0 μ and 826.8 μ, with a relative error of 1.805% at the starting position and −17.986% at the ending position. Near the weld center, mechanical behavior is complexly influenced by thermal expansion and contraction in the weld zone and the reaction binding force of the solid metal. Within a distance between −10 mm and 10 mm, and longitudinal stress is in a tension state, transverse stress fluctuates with a high gradient (~100 MPa).

Keywords: laser welding; transient strain; residual stress; deformation; aluminum alloy

Citation: Rong, Y.; Huang, Y.; Wang, L. Evolution Mechanism of Transient Strain and Residual Stress Distribution in Al 6061 Laser Welding. *Crystals* **2021**, *11*, 205. https://doi.org/10.3390/cryst11020205

Academic Editor: Heinz-Günter Brokmeier

Received: 30 January 2021
Accepted: 17 February 2021
Published: 19 February 2021

1. Introduction

Aluminum alloys are widely used in structure manufacturing because of their advantages of weight reduction and energy saving. Welding processes of aluminum alloys, mainly including laser welding [1], arc welding [2], electron beam welding [3], and friction stir welding [4], are important for structure manufacturing, while the welding accuracy and the quality are areas of interest for many researchers and engineers.

Discussion topics regarding the welding of aluminum alloys include processing, weld defects, mechanical performance, etc. The influence of the welding direction on the microstructural characterization of aluminum alloy 5083 was researched in hybrid laser-arc welding [5]. The microstructure and mechanical properties of AA 3003 in underwater friction stir welding were discussed by comparison analysis [6]. A dissimilar joint of aluminum alloy 7075 and magnesium alloy AZ31 was obtained, while silicon carbide nanoparticles were embedded into the weldment [7]. Three-dimensional printing technology was applied to produce the structural part of high-strength aluminum alloy 7075 [8]. Through multi-phase simulation and experiment analysis, the spatter formation mechanism of an aluminum alloy was investigated in full [9] and partial [10] penetration laser welding. Keyhole instability and porosity formation behaviors were analyzed in laser welding of a dissimilar joint of aluminum alloy with steel [11]. Thermal-elastic-plastic finite element analysis (TEP-FEA) was used to predict laser welding deformation and residual stress with a lap joint [12]. The measurement accuracy of residual stress was discussed in X-ray diffraction with different crystal planes [13], while strain gauges were used to observe and

obtain real-time strain values near the weld [14]. Inhomogeneous behavior of the meso-mechanical stress among joint microstructures was researched by a multiscale simulation method [15]. Mechanical properties, including tensile strength, fracture toughness, and hardness, were studied in hybrid laser-metal-inert-gas welding [16]. A criterion for solidification cracking and elimination by suitably ramping down the laser pulse was proposed in laser welding of 2024 aluminum alloy [17]. Laser oscillating welding was used to stir the weld pool and keyhole to improve the weld morphologies and refine grain size [18], and post-weld heat treatment was applied to homogenize the joint microstructure and improve the corrosion resistance [19]. Effects of weld penetration on the tensile properties of aluminum alloy welded joints were analyzed [20], and the fatigue damage mechanism of the T-joint was also researched [21].

In the above published works, thorough investigations into aluminum alloy welding have been carried out. Originating from the unbalanced procedure of melting and solidification, inhomogeneous mechanical behaviors in laser welding are intensified, especially residual stress and deformation. TEP-FEA was used by Lu et al. to analyze distributions of residual stress and deformation in arc welding of 5A06 aluminum alloy [22]. The stress evolution procedure was simulated by TEP-FEA and verified through a hole-drilling method [23]. Effects of welding parameters and welding sequence on residual stress and distortion were researched by Khosiroyan and Darvazi in Al6061-T6 aluminum alloy for a T-shaped welded joint [24], and a genetic algorithm was selected to optimize and mitigate the welding sequence with the goal of a low deformation [25]. Zhao et al. [26] analyzed the influences of the microstructure, defects, and stress distribution on the shear performance of the T-joints, and found that the formation of the equiaxed zone and high stress together contribute to the origin of shear fracture.

However, the reporting on transient strain and residual stress behaviors in laser welding of aluminum alloys is insufficient, and this is the focus of the present paper. The investigation framework is shown in Figure 1. Combining experiment analysis and TEP-FEA simulation, thermal-mechanical behaviors (temperature-induced weld profile, transient strain, residual stress, and deformation) are investigated to reveal their evolution mechanism in laser welding of aluminum alloys.

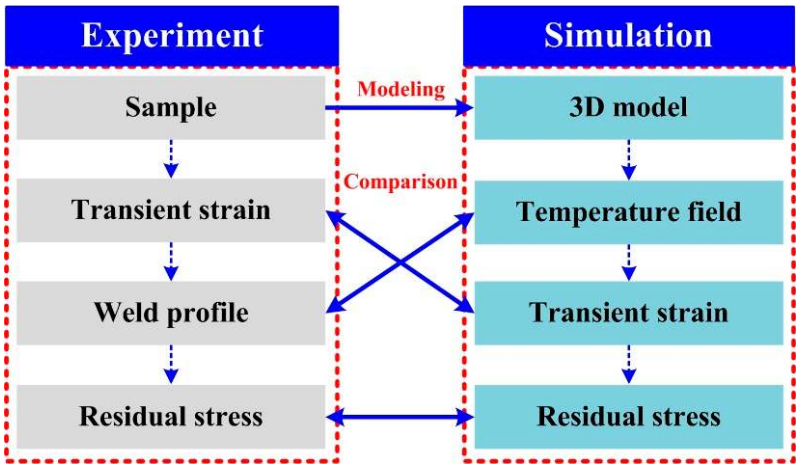

Figure 1. Investigation framework of this work.

2. Experiment and Measurement

2.1. Materials and Experimental Procedures

Aluminum alloy 6061 was selected as a base metal, and its chemical composition [24] and temperature-dependent mechanical properties [27] are given in Tables 1 and 2. The welded plate was designed with a size of 100 × 100 × 3 mm. The laser welding system is given in Figure 2. The plate sample was placed on the platform with a free state. Patch locations and welding path were planned based on the scribing method, and this

experiment was carried out once. A group of welding parameters with a good weld formation was selected through several attempts with their different combinations. Laser power was 2.7 kW, welding speed was 1.8 m/min, defocus length was 0 mm. Transient strains were extracted by an acquisition instrument and displayed on the computer, while the sampling frequency was 2000 Hz.

Table 1. Chemical composition of aluminum alloy 6061 (wt.%) [24].

Al	Si	Mg	Cu	Fe	Mn	Zn	Ti
97.63	0.561	0.986	0.31	0.289	0.052	0.024	0.018

Table 2. Temperature-dependent properties of aluminum alloy 6061 [27].

Temperature (°C)	Density ($kg \cdot m^{-3}$)	Heat Conductivity ($W \cdot m^{-1} \cdot °C^{-1}$)	Specific Heat Capacity ($J \cdot kg^{-1} \cdot °C^{-1}$)	Expansion Coefficient ($10^{-6} \cdot °C^{-1}$)	Elastic Modulus (GPa)	Yield Stress (MPa)
20.0	2700	162	945	23.45	68.54	274.4
93.3	2685	177	978	24.61	66.19	264.6
204.4	2657	192	1028	26.60	59.16	218.6
260.0	2657	201	1052	27.56	53.99	159.7
371.0	2630	217	1104	29.57	40.34	36.84
482.2	2602	226	1136	31.71	20.2	10.49

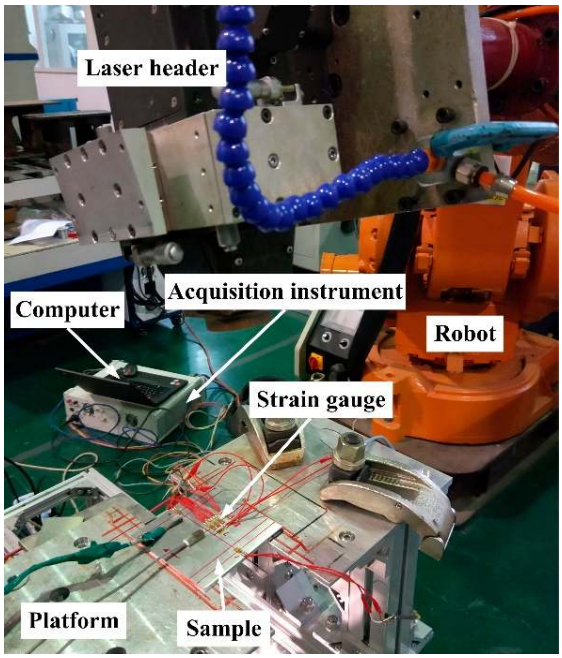

Figure 2. Laser welding system.

2.2. Measurement Methods

Strain gauge BHF 350-3AA with electrical resistance of 350 Ω was applied to extract transient strain in laser welding of aluminum alloy 6061, while its grille material was constant an alloy. As shown in Figure 3a, four strain gauges were pasted on the upper surface of the sample to extract transient strain values along longitudinal and transverse directions. 1# and 2# strain gauges were used to recognize longitudinal strain values at the starting and ending welding positions. Longitudinal strain was observed by 3# strain gauge along L1. 4# strain gauge was applied to measure transverse strains along L2. The acquisition circuit is given in Figure 3b. One end of the strain gauge was connected to the positive pole of bridge voltage with a value of 2 V (BV+), and another end was

simultaneously jointed to the positive pole of the strain-induced voltage signal (VS+) and 1/4 bridge (BR).

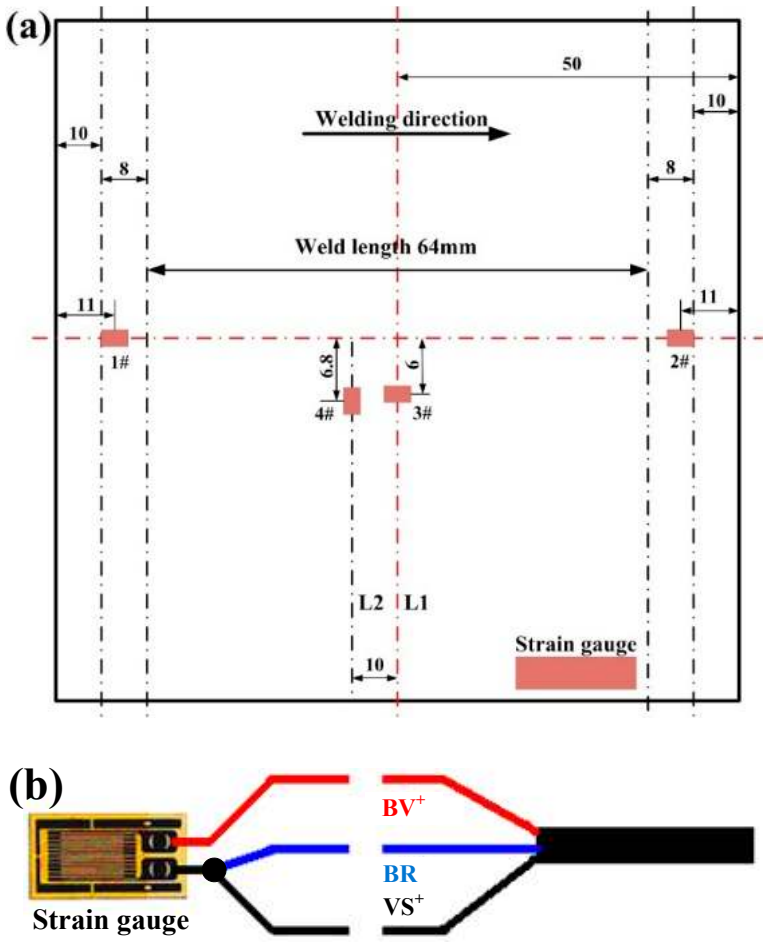

Figure 3. Measuring transient strain: (**a**) measurement points on the sample and (**b**) basic theory.

Residual stress was detected by X-ray diffraction technology. Multiple Ψ method was selected, while Ψ was the angle between the specimen normal and the direction of strain measurement. Characteristic ray Cr Kα was applied in the measurement process. The voltage and current of the X-ray tube were 25 kV and 5 mA. The weld profile was observed by an optical microscope, and after that a metallographic specimen was obtained by wire electrical discharge machining and then grinding-polishing-etching treatment.

3. Modeling and Simulation

3.1. TEP-FEA Framework

TEP-FEA is developed to simulate the thermal-induced mechanical behaviors in laser welding of an aluminum alloy, and the procedure is given in Figure 4. Considering a good reconstruction ability of the B-spline curve, the actual weld profile is fitted to load the simplified heat source model of laser power. In previously published articles by our team [28,29], TEP-FEA has been described in much more detail, and only the key points are emphasized here in the present work. Using the sequential coupling method, the temperature field is connected to the mechanical field by loading the thermal force of each increment.

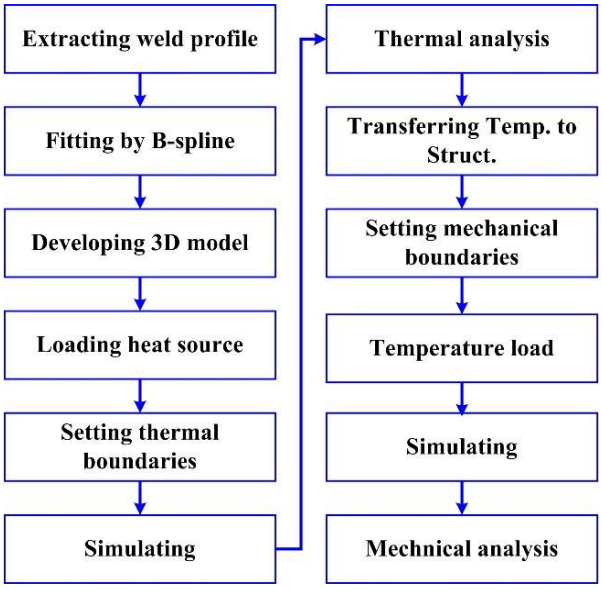

Figure 4. Thermal-elastic-plastic finite element analysis (TEP-FEA) procedure.

Based on the experiment setup in Section 2.1, the whole three-dimensional (3D) model is developed using ANSYS parametric design language (APDL). As shown in Figure 5, dense-to-sparse element distribution is designed from the weld sample center to edge, and a hexahedral element with 8 nodes is selected. Element types of thermal analysis and mechanical analysis are SOLID 70 and SOLID 185. Number of elements and nodes is 43,112 and 49,177, respectively. Displacement constraints of three points (Ux = Uy = Uz = 0, Uy = Uz = 0, and Uy = 0) are added to avoid rigid displacement and ensure FEA convergence.

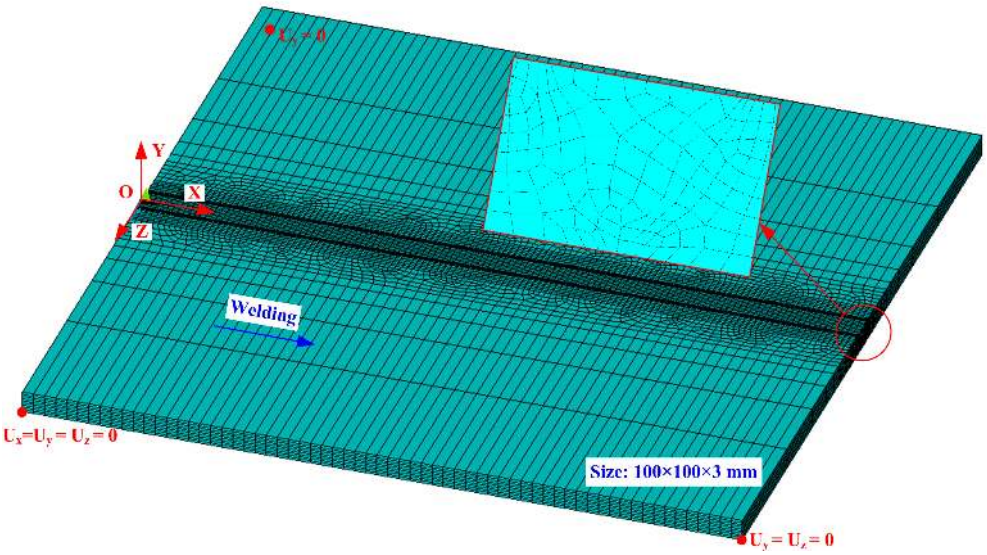

Figure 5. 3D mesh and free state.

3.2. Thermal Analysis Method

In the thermal analysis stage, Fourier's thermal conduction law is used to describe time-dependent temperature behavior, and its equation is given in Equation (1) [28].

$$\rho(T)c_p(T)\frac{\partial T}{\partial t} = k(T)[\frac{\partial}{\partial x}(\frac{\partial T}{\partial x}) + \frac{\partial}{\partial y}(\frac{\partial T}{\partial y}) + \frac{\partial}{\partial z}(\frac{\partial T}{\partial z})] + q(x,y,z) \quad (1)$$

where $\rho(T)$, $c_p(T)$, and $k(T)$, are density, specific heat capacity, and thermal conductivity. $q(x,y,z)$ is the input thermal flux, and its expression is given in Equation (2) [28].

$$q = \frac{\eta P}{Av} \tag{2}$$

where η = 0.55 is the efficiency of the heat source in the laser welding of the aluminum alloy, P = 2.7 kW is laser welding power, v = 1.8 m/min is laser welding speed, A is the actual area of the weld zone, while its edge contour is reconstructed by a B-spline fitting curve (Equation (3)) [30] to improve the loading zone accuracy of the laser heat flux.

$$B(u) = \sum_{i=0}^{n} d_i N_{i,k}(u) \tag{3}$$

while the B-spline basis function is described as (Equations (4)–(6)).

$$N_{i,1}(u) = \begin{cases} 1 & u_i < x < u_{i+1} \\ 0 & Otherwise \end{cases} \tag{4}$$

$$N_{i,k}(u) = \frac{u - u_i}{u_{i+k-1} - u_i} N_{i,k-1}(u) + \frac{u_{i+k} - u}{u_{i+k} - u_{i+1}} N_{i+1,k-1}(u) \tag{5}$$

$$define \quad \frac{0}{0} = 0 \tag{6}$$

where d_i (i = 0, 1, . . . , n) is the ith control point, i is node number, k presents the number of specified basis functions, $N_{i,k}$ means the kth basis function of the B-spline, and u is the parameter sequence of the piecewise function. The whole fitting curve is divided into two parts that are respectively fitted using B-spline, while the number of control points is 6.

In the whole welding process, radiation losses dominate for higher temperatures near the weld zone and convection losses for lower temperatures away from the weld zone, and the heat loss is considered by the heat transfer coefficient h_c (Equation (7)) [28].

$$h_c = \begin{cases} 0.0668 \cdot T & \mathrm{W/(m^2 \cdot {}^\circ C)} \quad T < 500\ {}^\circ\mathrm{C} \\ 0.231 \cdot T - 82.1 & \mathrm{W/(m^2 \cdot {}^\circ C)} \quad T \geq 500\ {}^\circ\mathrm{C} \end{cases} \tag{7}$$

3.3. Mechanical Analysis Method

In the mechanical analysis stage, temperature-induced mechanical behavior is simulated by sequentially loading the transient temperature with time increment. As shown in Equation (8) [29], the total strain ε_{total} consists of thermal strain ε_T, elastic strain ε_e, and plastic strain ε_p, while phase transformation-induced volumetric change strain and plastic strain are ignored. ε_{total} will be assumed as an initial elastic strain to calculate stress and evaluate the mechanical state (elasticity or plastic) in the whole welding process.

$$\boldsymbol{\varepsilon}_{total} = \boldsymbol{\varepsilon}_T + \boldsymbol{\varepsilon}_e + \boldsymbol{\varepsilon}_p \tag{8}$$

According to the principle of virtual displacement, mapping from element displacement to element force is described in Equation (9) [29], and the whole sample can be assembled with each element based on the equilibrium state equation.

$$d\mathbf{F} = \int \mathbf{B}^T \mathbf{D} \mathbf{B} d\mathbf{u} d\Omega - \int \mathbf{B}^T \mathbf{C} d\mathbf{T} d\Omega \tag{9}$$

where $d\mathbf{F}$ is element force increment, $d\mathbf{u}$ is element displacement increment, $\mathbf{B}$ is displacement-strain matrix, $\mathbf{C}$ is temperature-stress matrix, and $\mathbf{D}$ is stiffness matrix. Kinematic hardening and von Mises yield criterion are selected in the mechanical analysis stage.

4. Results and Discussion

4.1. Reconstruction of Weld Profile by B-Spline Curve

The microstructure in laser welding of Al 6061 has been investigated in previous works [31–33]. As described in Figure 6, a narrow heat-affected zone was formed owing to the higher cooling rates of laser welding, and equiaxed grains were observed near the weld center line. Nuclei were observed at the origin of the equiaxed grain (as indicated by a yellow dashed circle), which indicated that the equiaxed grain originates from heterogeneous nucleation. The reconstruction result of the weld profile by B-spline curve is shown in Figure 7. The actual weld geometry was inhomogeneous, and difficult to reconstruct by regular mathematical expressions to load the efficient heat source model in TEP-FEA. A B-spline curve was first used to reconstruct the actual weld profile, which was an accurate loading zone of the equivalent input laser power in the thermal simulation stage. The fitting result of the weld profile was marked by the red line, and the boundary between the fusion zone and base metal was noted by the blue dotted line. The fitting curve kept a good consistency with the actual weld profile, especially at the lower part of the whole weld. Maximum fitting deviation was 0.13 mm, and this mainly existed at the upper part and was pointed out by two grey elliptical regions. The fitting error was mainly sourced from the number and position limitations of control points.

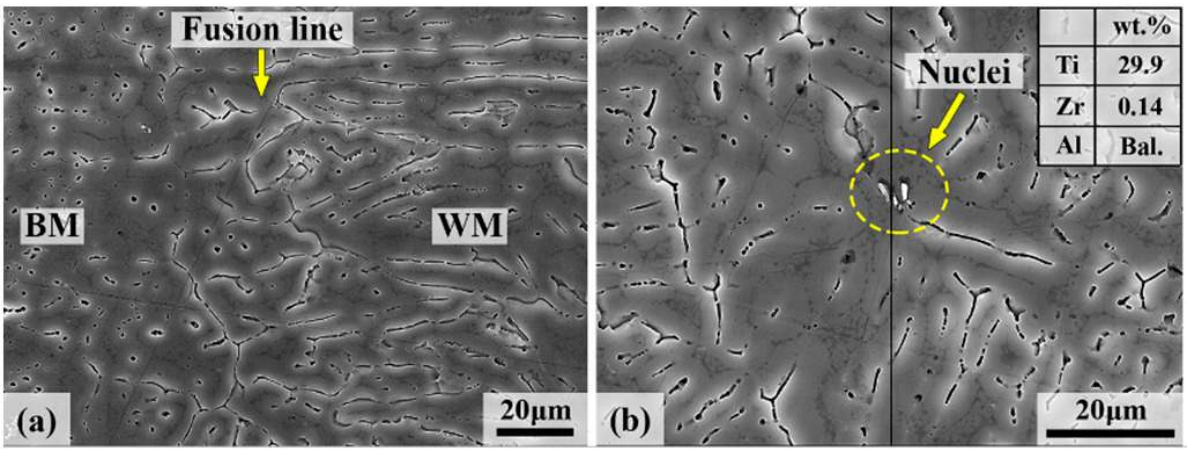

Figure 6. Microstructure of Al 6061 in laser welding: (**a**) near the fusion line, (**b**) heterogeneous nuclei [31].

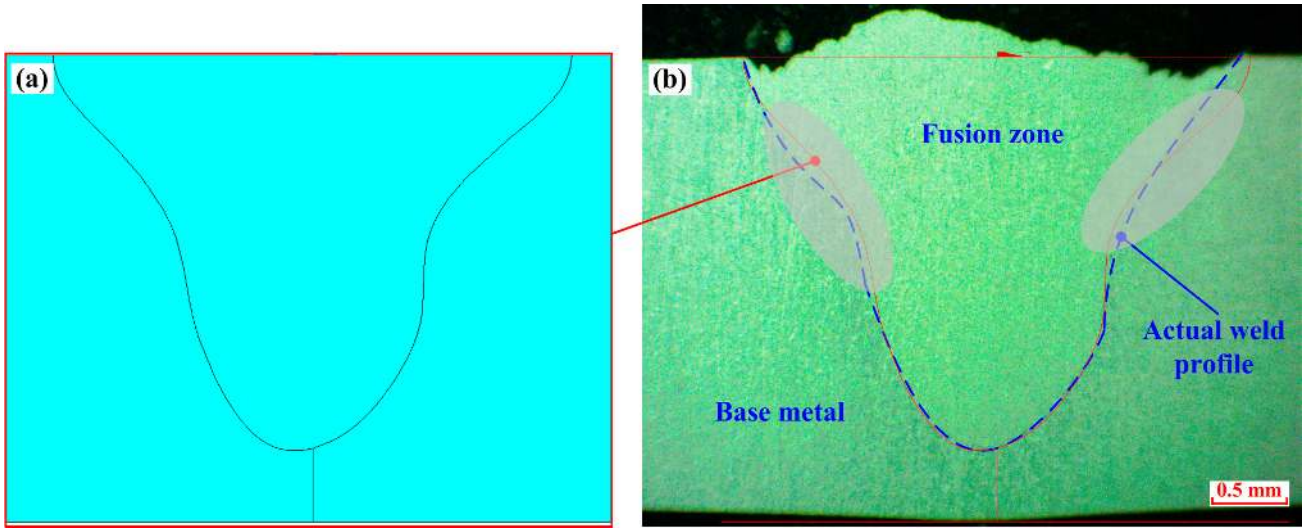

Figure 7. Fitting result of weld profile by B-spline curve: (**a**) reconstruction results of the weld profile, (**b**) Comparison results of experiment and fitting curves.

4.2. Fluctuation Analysis of the Transient Strain

Experiment extraction (time interval: 0.0005 s) and FEA simulation results are shown in Figure 8. Fluctuation curves of longitudinal strain at 1# and 2# are displayed in Figure 8a. At point 1#, the transient curve of the experimental result kept a slightly higher trend than that of the simulation result. Experimental and simulation results of residual strain were 842.0 μ and 826.8 μ, with a relative error 1.805%. At point 2#, coincidence between the experimental result and simulation result was maintained well before 3.5 s, values of the simulation result were then obviously higher than that of the experimental result, and relative error was −17.986% (experiment: 1239.3 μ, simulation: 826.8 μ). A common characteristic of 1# and 2# was that the time-dependent strain along the longitudinal direction started from a fluctuating compressive state and progressed to an ultimately stable tension state.

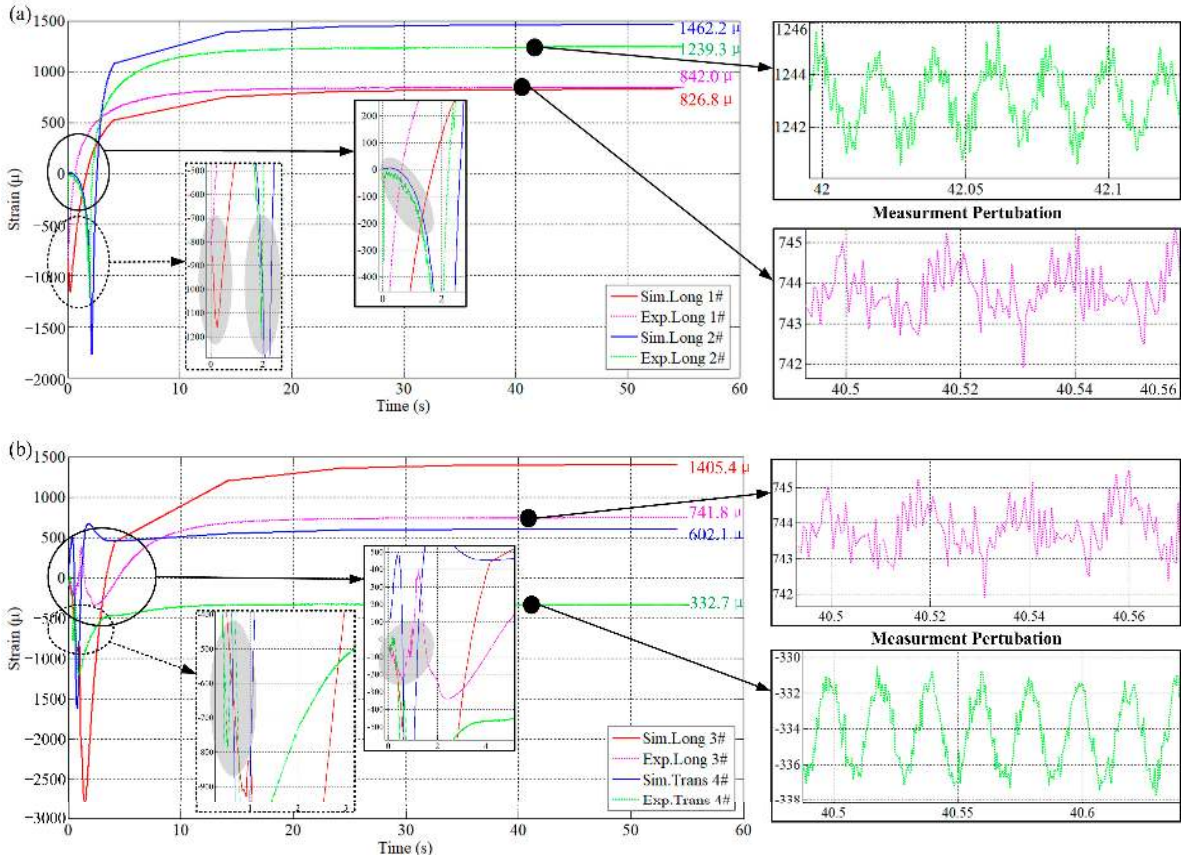

Figure 8. Transient strain of experiment and simulation results: (**a**) 1# and 2#, (**b**) 3# and 4#.

As shown in Figure 8b, at 3# and 4#, the mechanical state at measurement points was complexly influenced by thermal expansion and contraction in the weld zone and the reaction binding force of the solid metal. Longitudinal strain at 3# (1405.4 μ) and transverse strain at 4# (602.1 μ) were both nearly twice as high as experiment measurement results (741.8 μ and 332.7 μ), because liquid flow in the weld pool was ignored in TEP-FEA. Through local enlargement of measurement results after full cooling, it was clear that periodic fluctuation of strain came from the complex signal interference, and variation amplitude was less than 6 μ.

4.3. Discussion of Evolution Mechanism of Transient Strain

In the heating stage of laser welding, transient strain is the first response of input laser heat; in the following cooling stage, stress and deformation are incrementally accumulated through elastic or coupling plastic behaviors. Discussion of the evolution mechanism of

transient strain is an important and fundamental step in the study of stress and deformation in laser welding. Based on the transient strain fluctuations of experimental measurement and FEA simulation as mentioned above, we attempted to explain the evolution mechanism from the view of the unbalanced procedure of melting and solidification, which was caused by the external laser beam and the fundamental driving force of inhomogeneous mechanical behaviors in laser welding of aluminum alloy 6061.

Figure 9a shows the strain evolution process at 1#. The external laser beam with high thermal density interacted with the base metal, compression force was produced by phase transformation from solid base metal to liquid weld pool, and stretching force was further introduced in the cooling stage. This cyclic process can be used to reveal the strain fluctuation from a compressive state to a residual tension state in Figure 8a. Evolution mechanism at 2# (Figure 9b) was similar to that at 1#, and it is not necessary to describe it in detail. However, the fluctuation degree and residual value of strain at 2# were both higher than that at 1#, because the effective influence zone of melting-solidification cycle on 2# strain variation was the weld pool front wall and wider than that on 1#, and the temperature peak and heating-cooling rate were also obviously intense.

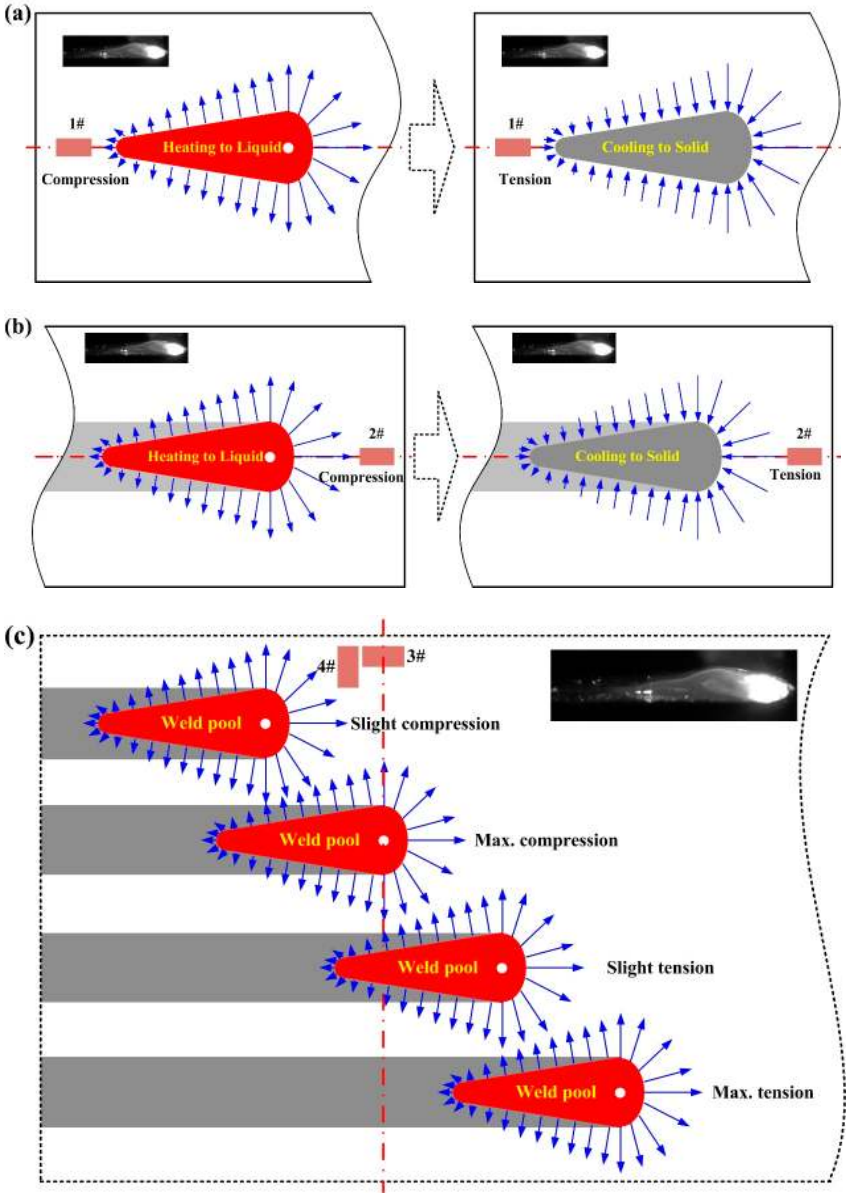

Figure 9. Formation procedure of transient strain for (**a**) 1#, (**b**) 2#, and (**c**) 3# and 4#.

The evolution process of transient strain at 3# and 4# is shown in Figure 9c. Strain state was directly influenced by relative position between measurement point and weld pool. Compression force came from the liquid weld pool, tension force was attributed to weld solidification, and the solid base metal around the measurement position also produced inner reaction force to keep a mechanical equilibrium state. Thus, it was difficult to accurately simulate time-dependent strain at 3# and 4# under a complex coupling state of compression and tension, especially when the flow of the weld pool was ignored in TEP-FEA.

4.4. Residual Distortion and Stress Analysis

Residual deformation of the whole weld sample is given in Figure 10. Deformations along different directions were unified under the same ruler (−0.3–0.3 mm). Ux along the welding direction was between −0.05897 and 0.01273 mm, Uy along the thickness direction was from −0.26459 to 0.06539 mm, Uz along the transverse direction ranged from −0.05107 to 0.07833 mm, and the maximum deformation sum was 0.26897 mm. Residual stress distributions and values are displayed in Figure 11 and Table 3. Sx was mainly in a tensile stress state at the weld area, and its maximum value (367.45 MPa) was measured at the ending welding zone. Fluctuation of Sy was obviously more moderate than that of Sx and Sz. Symmetric distribution of Sz around the transverse center line of the weld sample was presented, while amplitude and size of the compression stress zone at 2# were both larger than that at 1#, and maximum tensile stress (244.95 MPa) appeared nearly at the ending welding position. Equivalent stress based on von Mises (Seqv) was concentrated on the weld and its adjacent zone, and an apparent stress concentration appeared at the starting and ending welding positions.

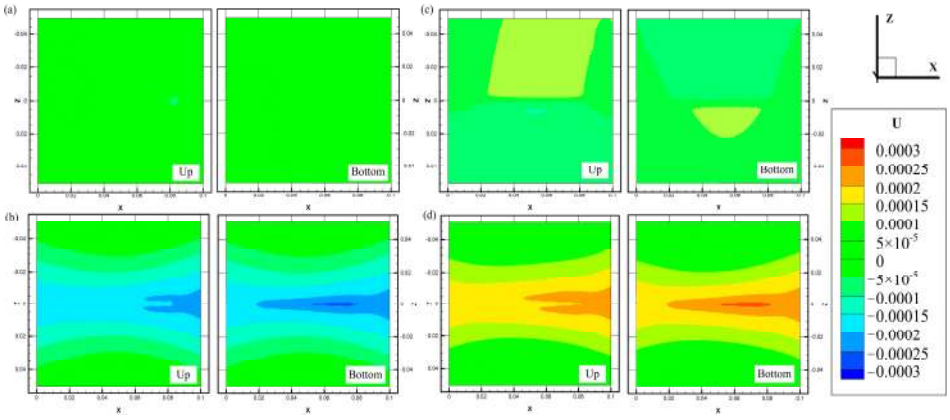

Figure 10. Residual deformation of the whole weld sample: (**a**) Ux, (**b**) Uy, (**c**) Uz, and (**d**) Usum.

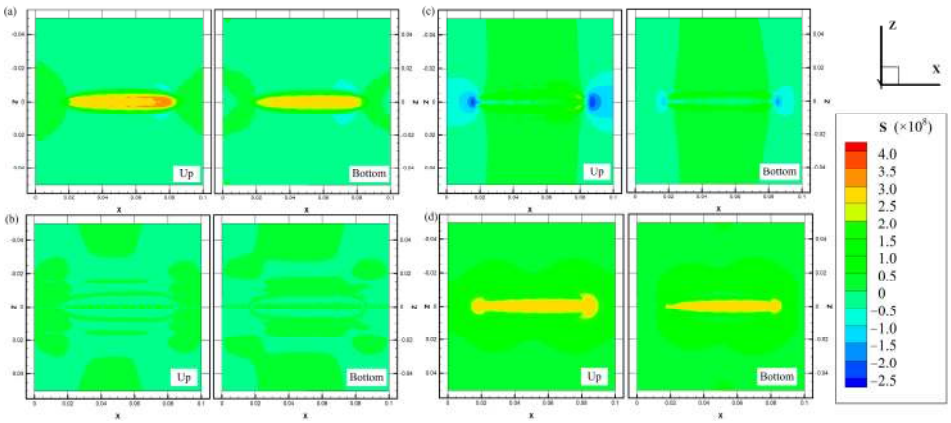

Figure 11. Residual stress of the whole weld sample: (**a**) Sx, (**b**) Sy, (**c**) Sz, and (**d**) Seqv.

Table 3. Maximum and minimum values of residual stress.

NO.	Stress Direction	Symbol	Residual Stress (MPa)	
			Min.	Max.
1	Longitudinal direction	Sx	−77.65	367.45
2	Thickness direction	Sy	−62.45	86.11
3	Transverse direction	Sz	−242.89	244.95
4	Equivalent stress	Seqv	3.96	278.24

Furthermore, fluctuation curves of angular distortion and stress along the transverse center line of the weld sample L1 are drawn in Figures 12 and 13. Angular distortions along the up surface and bottom surface were both displayed with some difference, especially at the weld zone. Distortion degrees were 0.3167° and 0.3578°, while their average value was 0.33725°. It was clear that the angular distortion in laser welding of the aluminum alloy was very small. Longitudinal stress was in a tension state within a distance between −10 mm and 10 mm. With the help of the X-ray residual stress tester, the measurement result of longitudinal stress was similar to the TEP-FEA result at the weld center. In the range of −10 mm to 10 mm, transverse stress fluctuated greatly with a high gradient (~100 MPa). The tendency of equivalent stress was similar to that of transverse stress far from the weld center and longitudinal stress near the weld center.

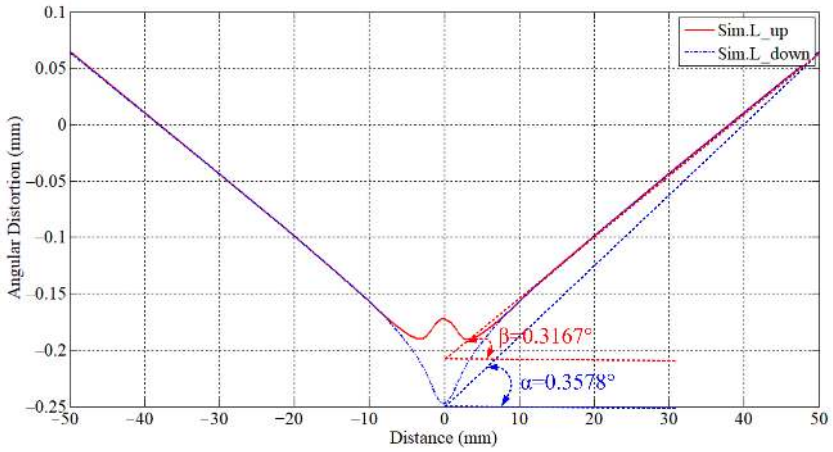

Figure 12. Angular distortion along L1.

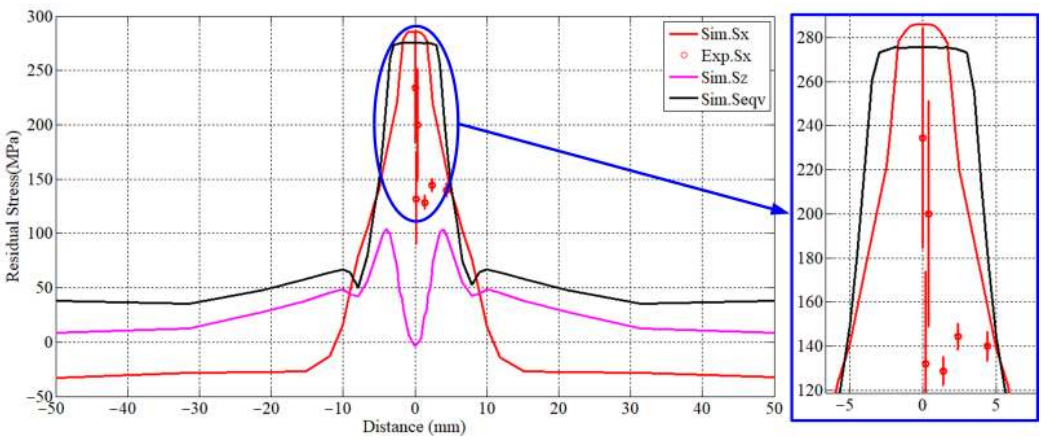

Figure 13. Residual stress along L1.

5. Conclusions

Combining experimental analysis with TEP-FEA, transient strain and residual stress were investigated in laser welding of Al 6061. The following four conclusions can be drawn:

(1) The actual weld profile was first fitted by a B-spline curve with 6 control points to load the efficient heat source model in TEP-FEA. The fitting profile kept a good consistency with the actual weld shape, especially at the lower part of the whole weld. A maximum fitting deviation of 0.13 mm was measured at the upper part, which was mainly due to the number and position limitations of control points.

(2) Fluctuation analysis of the transient strain at four points was investigated by coupling experimental analysis with TEP-FEA. A common characteristic of 1# and 2# was that longitudinal strain started from a fluctuating compressive state and progressed to an ultimate residual tension state. Experimental and simulation results of residual strain are 842.0 μ and 826.8 μ, with a relative error of 1.805% at the starting position and −17.986% at the ending position. At 3# and 4#, the mechanical state was complexly influenced by thermal expansion and contraction in the weld zone and the reaction binding force of the solid metal, and simulated strains were nearly twice as high as experiment results because liquid flow in the weld pool was ignored in TEP-FEA.

(3) The evolution mechanism of transient strain in laser welding of the aluminum alloy was also discussed in terms of the unbalanced procedure of melting and solidification, considering that it originated from the external laser beam and the fundamental driving force of inhomogeneous mechanical behaviors.

(4) Angular distortion along the transverse center line of the weld sample was 0.33725°. Longitudinal stress was in a tension state within a distance between −10 mm and 10 mm. In the range of −10 mm to 10 mm, transverse stress fluctuated greatly with a high gradient (~100 MPa). The tendency of equivalent stress was similar to that of transverse stress far from the weld center and longitudinal stress near the weld center.

Author Contributions: Conceptualization, Y.R. and Y.H.; methodology, Y.R.; software, Y.R.; data curation, L.W.; writing—original draft preparation, Y.R., Y.H., and L.W. All authors have read and agreed to the published version of the manuscript.

Funding: This research was funded by the National Natural Science Foundation of China, grant number 51905191; Key Research & Development Plan of Hubei Province, grant number 2020BAB051; Ministry of Industry and Information Technology special project for high-quality development of manufacturing industry, grant number TC200H02H; and Wuhan Science and Technology Planning Project, grant number 201903070311520.

Data Availability Statement: The data presented in this study are contained within this article.

Conflicts of Interest: The authors declare no conflict of interest.

References

1. Wang, L.; Wei, Y.; Chen, J.; Zhao, W. Macro-micro modeling and simulation on columnar grains growth in the laser welding pool of aluminum alloy. *Int. J. Heat Mass Transf.* **2018**, *123*, 826–838. [CrossRef]
2. Ye, Z.; Huang, J.; Cheng, Z.; Gao, W.; Zhang, Y.; Chen, S.; Yang, J. Combined effects of MIG and TIG arcs on weld appearance and interface properties in Al/steel double-sided butt welding-brazing. *J. Mater. Process. Technol.* **2017**, *250*, 25–34. [CrossRef]
3. Olshanskaya, T.V.; Salomatova, E.S.; Belenkiy, V.Y.; Trushnikov, D.N.; Permyakov, G.L. Electron beam welding of aluminum alloy AlMg6 with a dynamically positioned electron beam. *Int. J. Adv. Manuf. Technol.* **2017**, *89*, 3439–3450. [CrossRef]
4. Wang, Z.B.; He, Z.B.; Fan, X.B.; Zhou, L.; Lin, Y.L.; Yuan, S.J. High temperature deformation behavior of friction stir welded 2024-T4 aluminum alloy sheets. *J. Mater. Process. Technol.* **2017**, *247*, 184–191. [CrossRef]
5. Huang, L.; Wu, D.; Hua, X.; Liu, S.; Jiang, Z.; Li, F.; Wang, H.; Shi, S. Effect of the welding direction on the microstructural characterization in fiber laser-GMAW hybrid welding of 5083 aluminum alloy. *J. Manuf. Process.* **2018**, *31*, 514–522. [CrossRef]
6. Tan, Y.B.; Wang, X.M.; Ma, M.; Zhang, J.X.; Liu, W.C.; Fu, R.D.; Xiang, S. A study on microstructure and mechanical properties of AA 3003 aluminum alloy joints by underwater friction stir welding. *Mater. Charact.* **2017**, *127*, 41–52. [CrossRef]
7. Tabasi, M.; Farahani, M.; Givi, M.K.B.; Farzami, M.; Moharami, A. Dissimilar friction stir welding of 7075 aluminum alloy to AZ31 magnesium alloy using SiC nanoparticles. *Int. J. Adv. Manuf. Technol.* **2016**, *86*, 705–715. [CrossRef]

8. Martin, J.H.; Yahata, B.D.; Hundley, J.M.; Mayer, J.A.; Schaedler, T.A.; Pollock, T.M. 3D printing of high-strength aluminium alloys. *Nature* **2017**, *549*, 365–369. [CrossRef]
9. Wu, D.; Hua, X.; Huang, L.; Zhao, J. Numerical simulation of spatter formation during fiber laser welding of 5083 aluminum alloy at full penetration condition. *Opt. Laser Technol.* **2018**, *100*, 157–164. [CrossRef]
10. Zhang, D.; Li, C.; Liu, X.; Cao, Y.; Wu, D. Numerical study of spatter formation during fiber laser welding of aluminum alloy. *J. Manuf. Process.* **2018**, *31*, 72–79. [CrossRef]
11. Huang, L.; Hua, X.; Wu, D.; Li, F. Numerical study of keyhole instability and porosity formation mechanism in laser welding of aluminum alloy and steel. *J. Mater. Process. Technol.* **2018**, *252*, 421–431. [CrossRef]
12. Moraitis, G.A.; Labeas, G.N. Residual stress and distortion calculation of laser beam welding for aluminum lap joints. *J. Mater. Process. Technol.* **2008**, *198*, 260–269. [CrossRef]
13. Ji, P.; Zhang, J.; Zheng, L.; Xiao, Y.; Dou, S.; Cui, X.; Lian, Y. Comparison of residual stress determination using different crystal planes by short-wavelength X-ray diffraction in a friction-stir-welded aluminum alloy plate. *J. Mater. Sci.* **2017**, *52*, 12834–12847. [CrossRef]
14. Eisazadeh, H.; Aidun, D.K. Investigation of transient/residual strain and stress in dissimilar weld. *J. Manuf. Process.* **2017**, *26*, 372–381. [CrossRef]
15. Balokhonov, R.; Romanova, V.; Batukhtina, E.; Martynov, S.; Zinoviev, A.; Zinovieva, O. A mesomechanical analysis of the stress–strain localization in friction stir welds of polycrystalline aluminium alloys. *Meccanica* **2016**, *51*, 319–328. [CrossRef]
16. Wang, X.; Li, B.; Li, M.; Huang, C.; Chen, H. Study of local-zone microstructure, strength and fracture toughness of hybrid laser-metal-inert-gas-welded A7N01 aluminum alloy joint. *Mater. Sci. Eng. A Struct. Mater. Prop. Microstruct. Process.* **2017**, *688*, 114–122. [CrossRef]
17. Sheikhi, M.; Ghaini, F.M.; Assadi, H. Prediction of solidification cracking in pulsed laser welding of 2024 aluminum alloy. *Acta Mater.* **2015**, *82*, 491–502. [CrossRef]
18. Wang, L.; Gao, M.; Zhang, C.; Zeng, X. Effect of beam oscillating pattern on weld characterization of laser welding of AA6061-T6 aluminum alloy. *Mater. Des.* **2016**, *108*, 707–717. [CrossRef]
19. Zhu, Z.Y.; Deng, C.Y.; Wang, Y.; Yang, Z.W.; Ding, J.K.; Wang, D.P. Effect of post weld heat treatment on the microstructure and corrosion behavior of AA2219 aluminum alloy joints welded by variable polarity tungsten inert gas welding. *Mater. Des.* **2015**, *65*, 1075–1082. [CrossRef]
20. Zhang, D.K.; Zhao, Y.; Dong, M.Y.; Wang, G.Q.; Wu, A.P.; Shan, J.G.; Meng, D.Y.; Liu, X.L.; Song, J.L.; Zhang, Z.P. Effects of weld penetration on tensile properties of 2219 aluminum alloy TIG-welded joints. *Trans. Nonferrous Met. Soc. China* **2019**, *29*, 1161–1168. [CrossRef]
21. Duan, C.F.; Yang, S.L.; Gu, J.X.; Xiong, Q.; Wang, Y. Study on microstructure and fatigue damage mechanism of 6082 Aluminum Alloy T-Type Metal Inert Gas (MIG)Welded Joint. *Appl. Sci.* **2018**, *8*, 1741. [CrossRef]
22. Lu, N.C.; Wang, M.H.; Hao, G.D.; Wang, Y.T. Finite element analysis of residual welding stresses and deformation for a 5A06 aluminum alloy plate. *Strength Mater.* **2020**, *52*, 532–538. [CrossRef]
23. Nie, L.; Wu, Y.X.; Gong, H. Numerical Investigation on the Stress Evolution of Welding Process in Aluminium Alloy 2219. *Mechanika* **2019**, *25*, 57–63. [CrossRef]
24. Khosiroyan, A.; Darvazi, A.R. Effects of welding parameters and welding sequence on residual stress and distortion in Al6061-T6 aluminum alloy for T-shaped welded joint. *Trans. Nonferrous Met. Soc. China* **2020**, *30*, 76–89. [CrossRef]
25. Choi, M.; Wu, C.B.; Kim, J.W. Numerical Optimization of the Welding Sequence for Mitigating Welding Deformation in Aluminum Pipe Structures by Using a Genetic Algorithm. *Int. J. Precis. Eng. Manuf.* **2020**, *21*, 2323–2333. [CrossRef]
26. Zhao, Y.Q.; Zhan, X.H.; Chen, S.; Bai, M.Y.; Gong, X.R. Study on the shear performance and fracture mechanism of T-joints for 2219 aluminum alloy by dual laser-beam bilateral synchronous welding. *J. Alloy. Compd.* **2020**, *847*, 156511. [CrossRef]
27. Fu, D.F.; Zhou, C.Q.; Li, C.; Wang, G.; Li, L.X. Effect of welding sequence on residual stress in thin-walled octagonal pipe−plate structure. *Trans. Nonferrous Met. Soc. China* **2014**, *24*, 657–664. [CrossRef]
28. Rong, Y.; Xu, J.; Lei, T.; Huang, Y.; Shao, X.; Wang, C. Magnetism aided mitigation of deformation and residual stress in dissimilar joint 316L with EH36. *J. Mater. Process. Technol.* **2018**, *259*, 23–32. [CrossRef]
29. Rong, Y.; Lei, T.; Xu, J.; Huang, Y.; Wang, C. Residual stress modelling in laser welding marine steel EH36 considering a thermodynamics-based solid phase transformation. *Int. J. Mech. Sci.* **2018**, *146–147*, 180–190. [CrossRef]
30. Speleers, H. Algorithm 999: Computation of Multi-Degree B-Splines. *ACM Trans. Math. Softw.* **2019**, *45*, 43. [CrossRef]
31. Chu, Q.L.; Bai, R.X.; Jian, H.G.; Lei, Z.K.; Hu, N.; Yan, C. Microstructure in laser welding of Al 6061 beam welded joints. *Mater. Charact.* **2018**, *137*, 269–276. [CrossRef]
32. Kou, S.; Le, Y. Welding parameters and the grain structure of weld metal-A thermodynamic consideration. *Metall. Trans. A* **1988**, *19A*, 1075–1082. [CrossRef]
33. Zhang, C.; Gao, M.; Jiang, M.; Zeng, X.Y. Effect of weld characteristic on mechanical strength of laser-arc hybrid-welded Al-Mg-Si-Mn aluminum alloy. *Metall. Mater. Trans. A* **2016**, *47A*, 5438–5449. [CrossRef]